Available online at www.sciencedirect.com

ScienceDirect

journal homepage: www.elsevier.com/locate/he

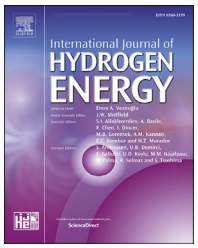

Experimental investigation of segmented SOECs: Locally-resolved impedance and degradation characteristics

Benjamin Königshofer [a,*], *Michael Höber* [a], *Norbert H. Menzler* [b], *Hartmuth Schröttner* [c], *Christoph Hochenauer* [a], *Vanja Subotić* [a]

[a] *Institute of Thermal Engineering, Graz University of Technology, Inffeldgasse 25/B, 8010 Graz, Austria*
[b] *Forschungzentrum Jülich GmbH, Institute of Energy and Climate Research (IEK-1: Materials Synthesis and Processing), 52425 Jülich, Germany*
[c] *Austrian Centre for Electron Microscopy and Nanoanalysis, Steyrergasse 17, 8010 Graz, Austria*

HIGHLIGHTS

- Locally resolved impedance and degradation characteristics of SOECs.
- Experimental results of SOECs performance under different operating conditions.
- Detailed insight into electrode processes and mechanisms via DRT and SEM analysis.

ARTICLE INFO

Article history:
Received 27 July 2022
Received in revised form
20 October 2022
Accepted 31 October 2022
Available online 17 November 2022

Keywords:
Solid oxide electrolysis cell (SOEC)
Segmented
Locally-resolved
Electrochemical analysis
Distribution of relaxation times (DRT)

ABSTRACT

High temperature solid oxide electrolysis cells (SOEC) provide an innovative solution for direct conversion of steam and electricity to hydrogen with the additional capability of adding CO_2 to produce syngas. However, specific operating conditions can have a negative impact on the performance and lifetime of SOECs. In this context, the distributions of operational parameters such as gas species, temperature and current density within the cell structure influence local transport processes and reaction kinetics and can lead to locally different electrochemical potentials and thus degradation phenomena. This study focuses on experimental investigations of steam-electrode supported SOECs with segmented air electrodes with the main objective to measure EIS and thus identify locally-resolved impedance and degradation characteristics caused by different operating conditions in steam and co-electrolysis mode. Thereby, significant correlations between operating conditions, local effects, electrode processes and degradation mechanisms were observed and analyzed in detail using EIS, DRT and SEM.

© 2022 The Author(s). Published by Elsevier Ltd on behalf of Hydrogen Energy Publications LLC. This is an open access article under the CC BY license (http://creativecommons.org/licenses/by/4.0/).

* *Corresponding author.*
E-mail address: benjamin.koenigshofer@tugraz.at (B. Königshofer).

https://doi.org/10.1016/j.ijhydene.2022.10.265

0360-3199/© 2022 The Author(s). Published by Elsevier Ltd on behalf of Hydrogen Energy Publications LLC. This is an open access article under the CC BY license (http://creativecommons.org/licenses/by/4.0/).

Introduction

In order to mitigate the threatening effects of the advancing climate change, greenhouse gas emissions must be drastically reduced and the further expansion of renewable energy sources is indispensable [1]. With the associated future increase in intermittent electricity generation, energy storage in the form of hydrogen and emerging hydrogen production technologies have recently attracted increasing interest [2,3]. High-temperature solid oxide electrolysis cells (SOECs) provide a practical solution for the direct conversion of steam and electricity to hydrogen [4], with the additional ability of adding CO_2 to the process to produce syngas [5,6], which can then be further processed into valuable liquid fuels [6,7]. With recent major improvements at cell, stack and system level, the SOEC technology is well on its way to achieving greater technological maturity [8,9].

However, different operating conditions are known to have a negative impact on the performance and lifetime of SOECs [10–12]. It is also known that the distribution of current, gas species, potential and temperature varies across the area of industrial-sized solid oxide cells [13,14]. In general, these distributions depend on transport phenomena such as mass, heat and charge transfer [15], which affect all chemical and electrochemical reactions across the cell [16,17]. In Refs. [18–20], the authors also discuss the negative effect of such local inhomogeneities on the long-term stability of SOECs. In order to gain a deeper insight into these local processes locally resolved current density, species and temperature distributions can be investigated using different simulation approaches. In this context, simulation studies focus on a wide range of areas such as the investigation of heat and mass transfer and electrochemical reactions [21], carbon capture and gasification mechanisms [22,23], flow configurations and electrical contact positions [20] and mechanical reliability and durability [24,25].

There are also a few studies that focus on the experimental investigation of the influence of various design-related parameters on local effects during solid oxide fuel cell (SOFC) operation. For example, the authors in Ref. [26] experimentally investigated the influence of different flow channel designs on the temperature distribution of SOFCs. In doing so, they proposed an alternative flow field design that offers a very homogeneous gas distribution as well as improved current collection at significantly lower manufacturing costs. Differently, the authors in Ref. [27] experimentally investigated the influence of different contacting methods on the long-term and thermal cycling stability of SOFCs. They found that current collection conditions significantly affect cell stability during thermal cycling and proposed an alternative in situ voltage measurement technique in order to assess the influence of different current collection types.

As these studies focus mainly on current, gas species and temperature distributions, it can be considered as crucial for the further development of the technology to extend the knowledge in this area to include the aspect of locally resolved impedance characteristics. However, the experimental studies required for this purpose require sophisticated cell and housing design as well as the proficient application of appropriate in situ characterization methods. Electrochemical impedance spectroscopy (EIS) has emerged as one such promising in situ characterization and online monitoring technique that can reliably determine performance changes [28–31] and degradation rates [32–34]. Further analysis of the impedance data using the distribution of relaxation times (DRT) allows the extraction of the most important time constants, which, if used appropriately, makes it even easier to track changes of different single or coupled processes within the SOEC [13,35,36]. This can be particularly useful for monitoring and interpreting small changes across the surface of a single cell. However, analyzing DRT spectra and assigning peaks to specific processes can be challenging.

Generally, the DRT peaks in the frequency range between 1 and 10 Hz are associated with gas diffusion overlapped with gas conversion impedance of the steam electrode [37–40]. The respective weighting of the influence of these processes on the peaks depends on the positioning of the peak, with conversion processes generally occurring at lower frequencies and diffusion processes at higher frequencies [41–45]. In addition, DRT peaks in the frequency range between 10 and 100 Hz can also be associated with gas diffusion in the steam electrode but overlapped with oxygen surface exchange and ion diffusion in the air electrode [39,40,46–49]. Thereby, the air electrode processes typically cover a wider frequency range between 10 and 500 Hz [37–39,42,43,45,50–52]. Furthermore, DRT peaks between 0.1 and 50 kHz can be associated with steam electrode processes such as gas diffusion, charge transfer reaction and ionic transport in the functional layer [37–39,41,43,53,54]. The higher frequency gas diffusion processes can mainly be linked to the lower part of this wide frequency range partly overlapping with the air electrode transport processes [47,48,53,54]. The charge transfer processes occur predominantly at higher frequencies between approximately 1 and 10 kHz overlapped with higher frequency gas diffusion processes [42,43,45–47,51,53,54]. The processes related to ionic transport in the functional layer are located at even higher frequencies between 10 and 50 kHz [42,43,51,53,55].

With proper application of this knowledge, it is feasible to correctly identify and interpret small differences in the EIS and DRT spectra, relate them to the specific processes and derive valuable information about the locally-resolved impedance and degradation behavior of SOEC.

Scope of this study

This study focuses on experimental investigations of steam-electrode supported SOECs with segmented air electrodes in stack-relevant size. The main objective is to identify locally-resolved impedance and degradation characteristics caused by different operating conditions during operation in steam and co-electrolysis mode. In this way, extensive electrochemical analyses using EIS and DRT were performed throughout the experiments, identifying significant correlations between local effects, operating conditions, electrode processes and degradation mechanisms.

Experimental setup

Cell design and housing

The experiments within this study were performed on steam-electrode supported SOEC single cells composed of a Ni-YSZ steam electrode support and a similar composed finder thin electrode, an YSZ electrolyte, a barrier layer made of Gd-doped ceria (GDC) and a segmented $La_{0.58}Sr_{0.4}Co_{0.2}Fe_{0.8}O_{3-\delta}$ (LSFC) air electrode. More details on the composition and thickness of the cell layers are described in Ref. [56]. Fig. 1a/1b show a schematic representation of the cell and flow configurations. The cells are 10 × 10 cm^2 in size, with the air electrode divided into four equal sections, each with an active area of 4.25 × 4.25 cm^2. The labels L-1/2 and R-1/2 refer to the four different segments of the cell. The entire air electrode area is contacted with a platinum mesh placed over all four segments and the inactive cross-shaped area between them. Separate sensing leads are attached to the outer corners of the mesh for each of the four segments. Eight platinum cables were mounted evenly along the outer rim of the mesh minimizing the influence of the current collection positions on the current distribution according to Ref. [20]. The cells were installed in a ceramic housing within the furnace of the test rig, which allows operation in co-, counter- and cross-flow by changing the direction of the air flow as presented in Fig. 1b. Within the ceramic cell housing, gases are distributed to both electrodes via gas flow channels. Multiple thermocouples (Type N) were positioned at the in- and outlets of the gas flows and within the ceramic plates. It should be mentioned that due to this positioning of the thermocouples within the ceramic plates, the relative changes in temperatures over time are more relevant than the absolute values. More details on the ceramic

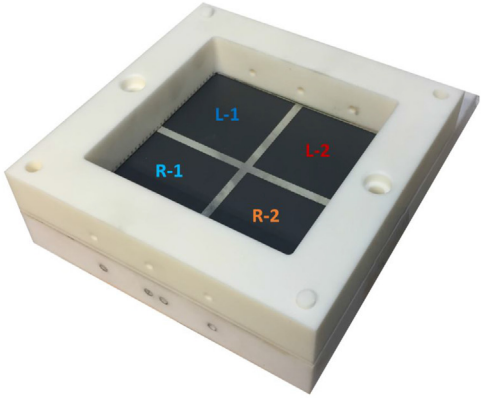

(a) Exemplary representation of the cell during installation in the cell housing.

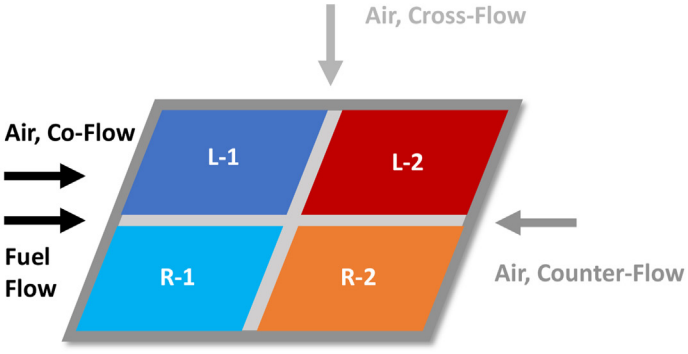

(b) Cell segments and flow configurations.

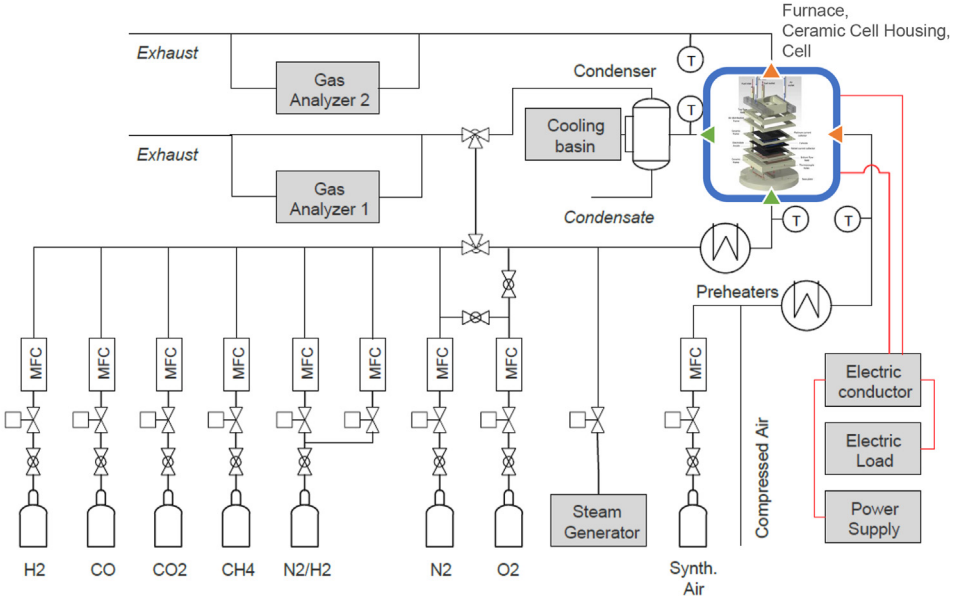

(c) Test rig. [28]

Fig. 1 – Experimental setup.

cell housing and the positioning of thermocouples are described in Ref. [57]. Additionally, the heat-up and reduction processes of the cells are described in Ref. [17].

Test rig

The scheme of the test rig used for the experiments is presented in Fig. 1c. A gas control system with mass flow controllers regulates the mixing of the inlet gas compositions, with a separate steam generator used for the production of steam. The inlet gas mixtures are then pre-heated up to temperatures >750 °C before entering the cell housing. The outlet gases pass through a water-cooled condenser to the exhaust. The test rig is further equipped with an electronic load, impedance analyzers and gas analyzers. More detailed information about the test rig can be found in Ref. [57].

(a) Exemplary representation of the cell during installation in the cell housing. (b) Cell segments and flow configurations. (c) Test rig [28].

Operating parameters

In this study different operating conditions were applied to single cells with segmented air electrodes in electrolysis mode. In order to investigate their influence on the cell's performance, the following parameters were varied during the experiments: gas inlet composition, temperature and current density. More details about the operating parameters are summarized in Tables 1 and 2. In this work, the labels containing "EC" refer to gas inlet mixtures with only steam as reactant. The labels containing "CO" describe gas inlet mixtures with steam and CO_2 as reactants and the labels containing "CC" refer to gas inlet mixtures with only CO_2 as an initial reactant. All labels also include a number indicating the relative amount of the specific reactant in the gas mixture.

Measurements and analysis methods

During the experiments the polarization curves were recorded with a current ramp of 10 A/min, whereby a moderate current ramp of 4 A/min was chosen for all other power supply changes. All operating temperature changes were conducted slowly with 1 K/min. After all experiments, a detailed post-mortem analysis was performed using a scanning electron microscope (SEM) and energy dispersive X-ray (EDS) analysis of the regions of interest.

In order to monitor the performance and state of health of the cell electrochemical impedance measurements (EIS) were performed throughout all experiments. The EIS measurements were performed in galvanostatic mode. Therefore, an alternating current with an amplitude of 4% of the applied direct current was superimposed on the direct current. The validity of the experimental data was checked by applying the Kramers-Kronig (KK) test and the Z-hit method, and further analysis of the data was performed only with data points that had a relative error of less than 4% between the original impedance and the impedance determined from the KK test. More detailed information is available in Refs. [58,59]. In this study, the impedance data are represented in Nyquist diagrams and by the distribution of relaxation times (DRT). More information about the method used for calculation of DRT used within this study can be found in Ref. [60].

Table 1 – Gas inlet mixtures.

Label	Fuel flow	H_2	H_2O	CO	CO_2	Air flow
	SLPM	%	%	%	%	SLPM
EC-50	2.0	50	50			2.0
CO-25	2.0	25	25	25	25	2.0
EC-90	2.0	10	90			2.0
CO-45	2.0	10	45		45	2.0
CC-90	2.0	10			90	2.0

Table 2 – Operating parameters.

Fig.	Mixture	Temp.	Current	Flow	Segment
		°C	mA/cm^2		
2	EC-50	800	0-400/350	Co	all
3	EC-90	750	150/300	Cross	L-1/R-2
4	CC-90	750	150/300	Cross	L-1/R-2
5	EC-50/EC-90	800	300	Cross	L-1/R-2
6	EC-90/CO-45	750	300	Cross	L-1/R-2
7	EC-50	750/800	300	Co	L-1/R-2
8	CO-25	750/800	300	Co	L-1/R-2
9	CC-90	750	250	Cross	L-1
9e	EC-90	750	250	Cross	L-1
10	CC-90	700	150	Cross	L-1
10e	EC-90	700	250	Cross	L-1

Results and discussion

This section summarizes the main results of the experimental campaign and presents and analyzes the impedance data in the form of Nyquist and DRT diagrams. In addition, the data are presented in the form of distribution plots, which were chosen as a descriptive representation to easily present local changes in ohmic and polarization resistance (△Ro and △Rp) based on interpolation between the four measurements taken at the corners of the cell (Fig. 1b). Thereby, the ohmic resistance values were determined at Z′ (Z" = 0) and the polarization resistance distribution was calculated between Z′ (Z" = 0) and Z' (f = 0.5 Hz). The colorbars of the distribution plots are scaled equally within each subsection in order to highlight the differences in changes between steam and co-electrolysis mode.

Fig. 2a and Fig. 2b show initial polarization curves and EIS curves recorded for the four segments during co-flow operation at EC-50 (1) and 800 °C. The OCV was 912.6 ± 0.9 mV, thus being largely uniform between the segments. These very small variations in OCV values indicate that only a minor influence can be attributed to differences in manufacturing, contacting, gas and temperature distribution. The performance of the fuel inlet segments (Fig. 1b, L-1/R-1) was slightly lower than that of the fuel outlet segments (Fig. 1b, L-2/R-2) with voltages of 1163.2 ± 1.82 mV for L-1/R-1 and 1151.2 ± 0.3 mV for L-2/R-2 at 400 mA/cm^2. The measured ohmic resistances for the fuel inlet segments ranged from 334 to 337 mΩ and from 285 to 286 for the fuel outlet segments,

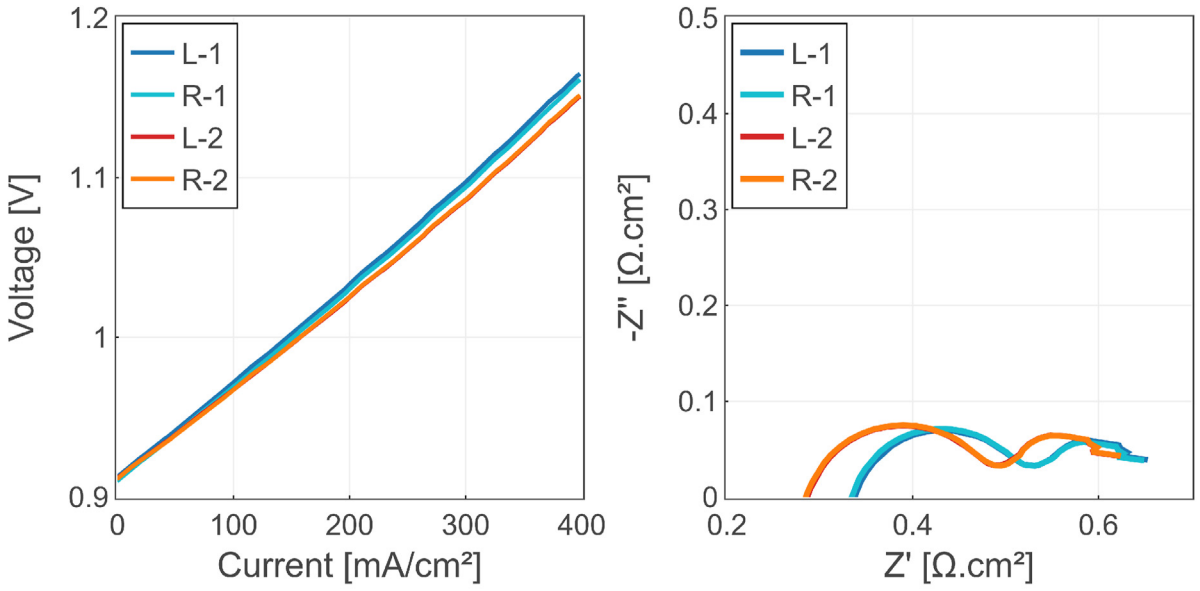

(a) Intial polarization curves (Co-Flow). (b) Intial EIS curves (Co-Flow) at 350 mA/cm^2.

Fig. 2 – Initial polarization curves and EIS curves. Labels L-1/2 and R-1/2 refer to the four segments (Fig. 1b).

respectively. Differently, the size of the low- and high-frequency arc was minimally larger for the fuel outlet segments. The difference in ohmic resistance was attributed to the temperature gradient along the length of the cell during electrolysis operation. The minimally larger low- and high-frequency arcs were mostly linked to the different local partial pressures of H_2 and H_2O in the steam electrode and O_2 in the air electrode.

Influence of current density

Fig. 3 presents the results from steam electrolysis operation with EC-90 at 750 °C and different current densities. Increasing the current density from 150 to 300 mA/cm^2 resulted in an increase of the size of the low-frequency arc and a slight decrease of the size of the high-frequency arc as shown in Fig. 3c. The ohmic resistance remained mostly unchanged between 545 mΩ cm^2 (L-1) and 512 mΩ cm^2 (R-2), whereby a slight decrease of −1.5% was observed for the gas outlet segments L-2/R-2 with increasing current density (Fig. 3a). The polarization resistance distribution (Fig. 3b) was calculated between Z′ (Z'' = 0) and Z' (f = 0.5 Hz), with the gas outlet segments L-2/R-2 presenting higher values of 13.0% compared to 10.5% for the inlet segments L-1/R-1. The decreasing ohmic resistance of the gas outlet segments L-2/R-2 was mainly attributed to the increasing temperature gradient along the cell length with increasing current density. The slightly higher increase in polarization resistance of the gas outlet segments is analyzed in detail with DRT data of segments L-1 (blue) and R-2 (orange) in Fig. 3d.

Increasing the current density from 150 to 300 mA/cm^2 resulted in a slight shift of the low-frequency (LF) peak from 16 to 19 Hz (L-1) and from 14 to 17 Hz (R-2). An additional small peak at 1 Hz was observed for the inlet segment (L-1) at 150 mA/cm^2, the occurrence of which was associated with inhibited diffusion and conversion processes due to minor inhomogeneities in the gas stream and mixture at the gas channel entry areas according to Ref. [23]. The shift of the LF peak towards higher frequencies as well as the disappearance of the small additional peak at L-1 and a small decrease of the amplitude at R-2 was interpreted to be linked to enhanced diffusion processes at higher current densities and higher hydrogen partial pressures according to Refs. [29,44,53]. Whereas peaks in this frequency range generally shift to higher frequency ranges when working with relatively high gas flow rates per cell area, according to Refs. [13,47,61]. The relatively small changes of this peak with increasing current density were further interpreted to result from the low conversion rates if compared to Refs. [29,61]. The amplitude of the mid-frequency (MF) DRT peak of segment L-1 slightly decreased from 0.91 to 0.74 mΩ with the peak shifting from 88 to 178 Hz. Similarly, the amplitude of MF peak of segment R-2 decreased from 0.95 to 0.84 mΩ with the peak shifting from 89 to 192 Hz. These changes were interpreted to be linked to enhanced air electrode transport processes as a result of the higher electrochemical reaction rate and higher oxygen partial pressures at the LSCF air electrode at higher current densities similar to the results in Ref. [62]. The first high-frequency (HF-1) DRT peak shifted from 503 to 623 Hz (L-1) and from 503 to 1023 Hz (R-2). The amplitudes of the peaks slightly decreased for both segments. The second high-frequency (HF-2) DRT peak shifted from 7.2 to 6.5 kHz (L-1) and from 7.8 to 7.6 Hz (R-2). The amplitudes of the peaks increased from 2.10 to 2.94 mΩ (L-1) and from 2.51 to 3.09 mΩ (R-2). Thereby, the larger shift of the HF-1 peak of the outlet segment (R-2) was mainly linked to enhanced gas diffusion

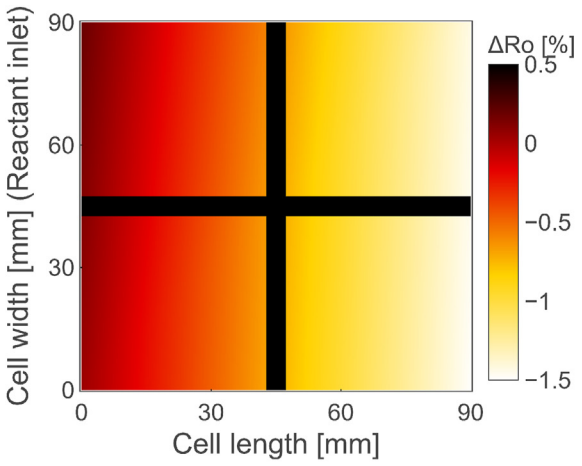

(a) Local changes of ohmic resistance (△Ro).

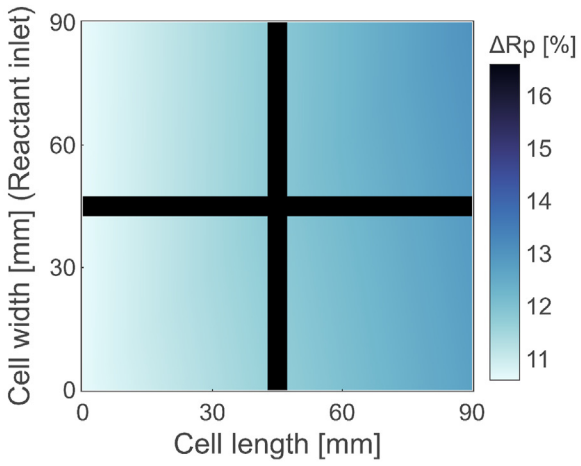

(b) Local changes of polarization resistance (△Rp).

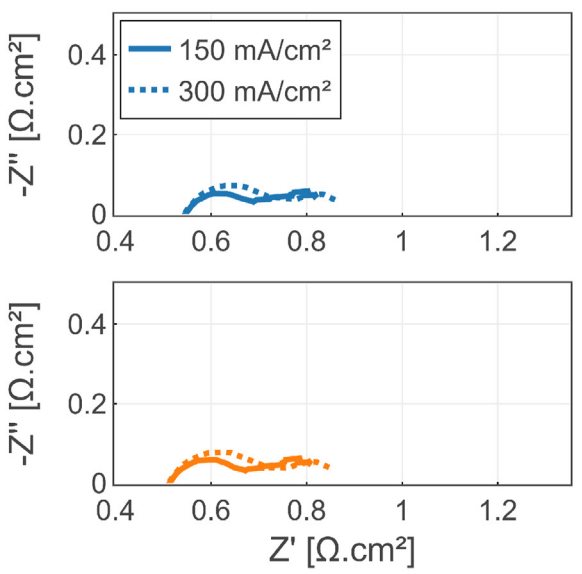

(c) EIS at different current densities (L-1: top/blue, R-2: bottom/orange).

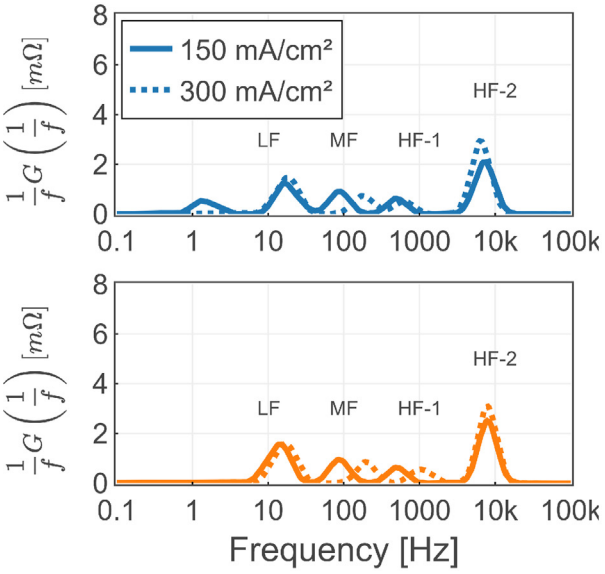

(d) DRT at different current densities (L-1: top/blue, R-2: bottom/orange).

Fig. 3 – Influence of increasing current density at EC-90 and 750 °C. (For interpretation of the references to color/colour in this figure legend, the reader is referred to the Web version of this article).

processes due to locally higher hydrogen partial pressures if compared to the inlet segment (L-1).

Fig. 4 presents the results from co-electrolysis operation with CC-90 at 750 °C and different current densities. Thereby, the ohmic resistance remained mostly constant at 555 mΩ cm^2 (Fig. 4c) when increasing current density from 150 to 300 mA/cm^2. Here, only a slight decrease was observed for the inlet segments (L-1/R-1) and slight increase was observed for the outlet segments (L-2/R-2) with increasing current density as presented in Fig. 4a. The polarization resistance significantly increased by more than 35% (Fig. 4b) with increasing current density, whereby a significant increase of the high-frequency arc and a slight decrease of the low-frequency arc were observed at presented in Fig. 4c. The higher increase in polarization resistance of the gas inlet segments is analyzed in detail with DRT data of segments L-1 (blue) and R-2 (orange) in Fig. 4d.

The LF peaks cover a significantly wider frequency range between 2.5 and 50 Hz if compared to the previous results. Here two major peaks were observed at 22 and 19 Hz for the segments L-1 and R-2, respectively. Increasing the current density from 150 to 300 mA/cm^2 resulted in a clearer formation of an additional low-frequency peak at approximately 5 Hz. The amplitude of MF peak of segment L-1 decreased from 0.97 to 0.47 mΩ with the peak shifting from 198 to 169 Hz. Similarly, the amplitude of MF peak of segment R-2 decreased from 0.93 to 0.54 mΩ with the frequency remaining unchanged. The HF peaks range cover a wide

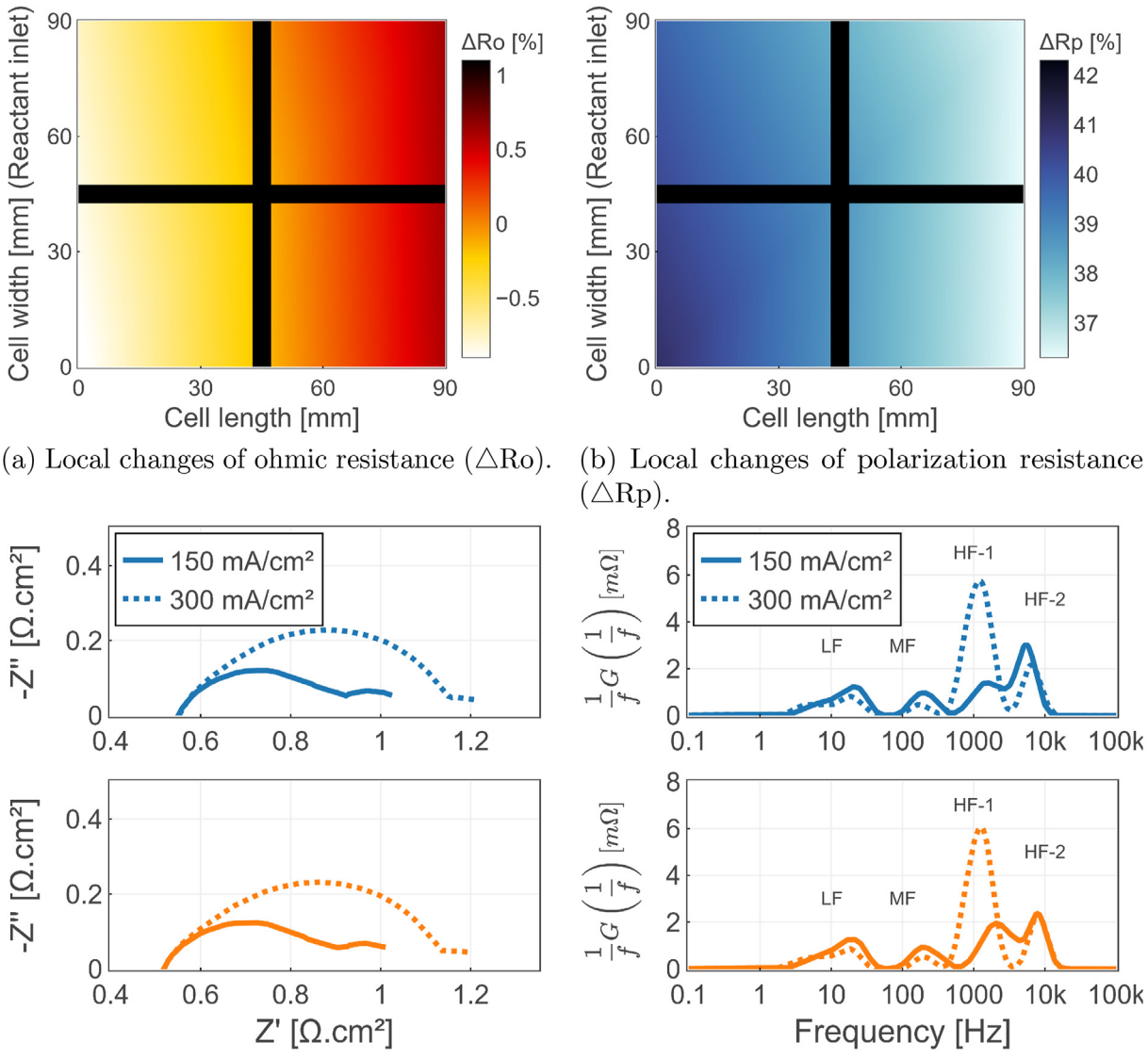

(a) Local changes of ohmic resistance (△Ro).

(b) Local changes of polarization resistance (△Rp).

(c) EIS at different current densities (L-1: top/blue, R-2: bottom/orange).

(d) DRT at different current densities (L-1: top/blue, R-2: bottom/orange).

Fig. 4 – Influence of increasing current density at CC-90 and 750 °C. (For interpretation of the references to color/colour in this figure legend, the reader is referred to the Web version of this article).

frequency range between 0.5 and 10 kHz with no clear separation of the peaks at 150 mA/cm^2. At 300 mA/cm^2 two separated HF peaks at 1200 and 6600 Hz (L-1) as well as 1250 and 8000 Hz (R-2) with slightly higher amplitudes at the outlet segments can be observed.

Generally, the mass transfer and diffusion losses for CO_2-electrolysis are considered to be higher than for steam electrolysis [21,63]. Therefore, more heat is generated by irreversible overvoltage losses in CO_2-electrolysis than in steam electrolysis for the same current density [21]. This was considered to be the main influence on the opposite trend of local changes in ohmic resistance (Fig. 4a) for steam and co-electrolysis. The relatively higher increase of the polarization resistance when increasing current density was also interpreted to be linked to the higher mass transfer and diffusion losses for co-electrolysis. These changes are also visible in Fig. 4d with the formation of the dominant HF peak at approximately 1 kHz suggesting inhibited gas diffusion and charge transfer reaction [39,43,64,65]. Also, the development of the low-frequency peak at 5 Hz could be linked to inhibited conversion processes in the steam electrode [42–44]. As a result of the comparatively slower mass transfer from CO_2 to the TPB and the slower diffusion of CO [21], an increase in current density was interpreted as having a negative effect on local conversion rates, especially for the inlet regions of the cell (Fig. 4b). This effect is weakened when the CO_2/CO ratio decreases along the cell length and thus the diffusivity of the gas mixture increases.

Influence of inlet gas composition

Fig. 5 presents the results from steam electrolysis operation at 300 mA/cm^2 and 800 °C with different H_2O/H_2-ratios. Thereby, the H_2O/H_2-ratio was changed from 50/50 (EC-50) to 90/10 (EC-90). Increasing the H_2O/H_2-ratio resulted in an increase of the ohmic resistance with higher value for the outlet segments (Fig. 5a) and a locally uniform decrease of the polarization resistance (Fig. 5b). Analysis of the impedance data further showed a decrease of the size of the low-frequency arc as well as an increase of the size of the high-frequency arc (Fig. 5c). The LF peaks of both segments stayed at approximately 15 Hz with a minor increase of the amplitudes with increasing H_2O/H_2-ratio. An additional small peak occurred at 1 Hz for operation at EC-90. Generally, higher absolute values were observed for the outlet segment. The MF peak of the inlet segment (L-1) shifted from 591 to 364 Hz and from 0.37 to 0.41 mΩ. Differently the MF peak of the outlet segment (R-1) split from 817 Hz to 0.53 mΩ into two new peaks at 264 and 641 Hz and 0.22–0.33 mΩ. The HF peaks of both segments shifted towards higher frequencies and low amplitudes, whereby again higher frequencies and amplitudes were observed for the outlet segment.

The increase of ohmic resistance can mainly be linked to significantly lower cell temperatures at EC-90 with the thermal equilibrium dominated by the endothermic electrolysis

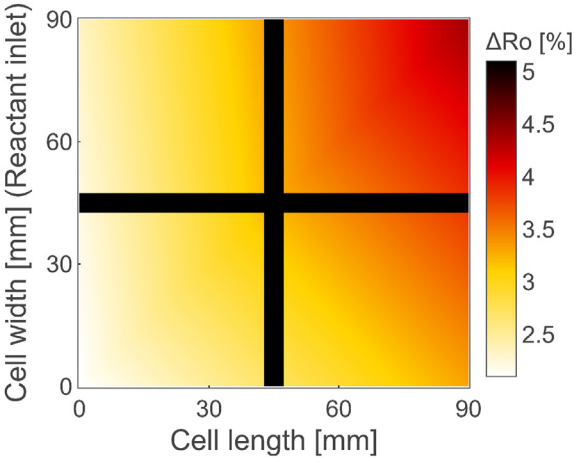

(a) Local changes of ohmic resistance (△Ro).

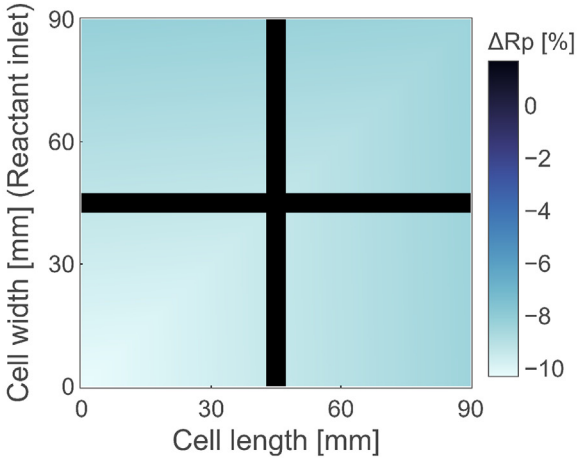

(b) Local changes of polarization resistance (△Rp).

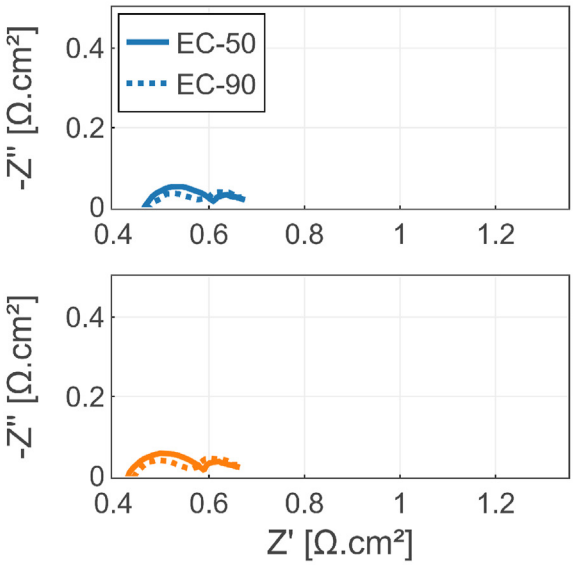

(c) EIS at different steam contents (L-1: top/blue, R-2: bottom/orange).

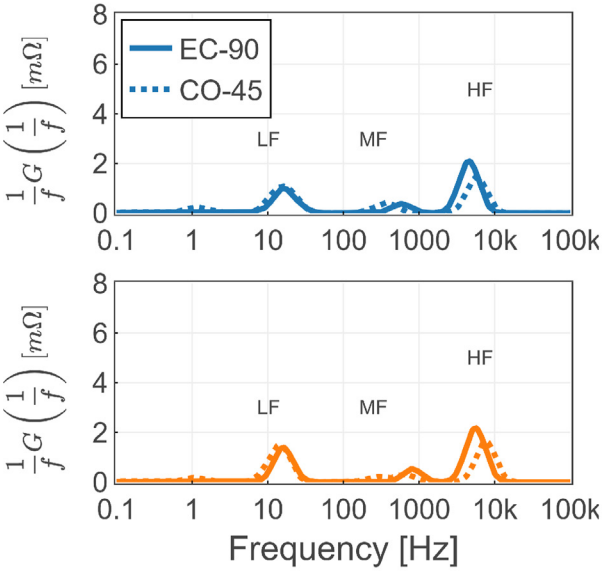

(d) DRT at different steam contents (L-1: top/blue, R-2: bottom/orange).

Fig. 5 – Influence of increasing steam content at 300 mA/cm^2 and 800 °C (EC-50/EC-90). (For interpretation of the references to color/colour in this figure legend, the reader is referred to the Web version of this article).

reaction with less influence of the overvoltage losses compared to operation at EC-50. The relatively higher increase of the ohmic resistance for the outlet segment could also be interpreted to be the result of a non-uniform temperature distribution resulting from significantly different species gradients along the cell length during operation at EC-90. The shift of the LF peak towards slightly higher amplitudes as well as the occurrence of the additional small peak at 1 Hz was interpreted to be linked to changes in effective diffusivity of the inlet gas composition according to Refs. [37,53]. The changes of the MF peaks could indicate a clearer separation of the high frequency gas diffusion processes from the air electrode transport processes which are dominant in this frequency area according to Refs. [47,48,53,54]. The high frequency charge transfer processes present a strong dependency on the temperature which was 10–15 °C higher at the L-1 segment during operation at EC-50 compared to EC-90. These processes also present a minor dependency on steam partial pressure which shifts the HF peak towards higher frequencies and lower amplitudes during operation at EC-90 according to Ref. [47].

Fig. 6 presents the results from steam and co-electrolysis operation at 300 mA/cm^2 and 750 °C with different inlet gas compositions. Thereby, the $H_2O/CO_2/H_2$-ratio was changed from 90/0/10 (EC-90) to 45/45/10 (CO-45). Thereby, a small increase of the ohmic resistance which was uniform over the

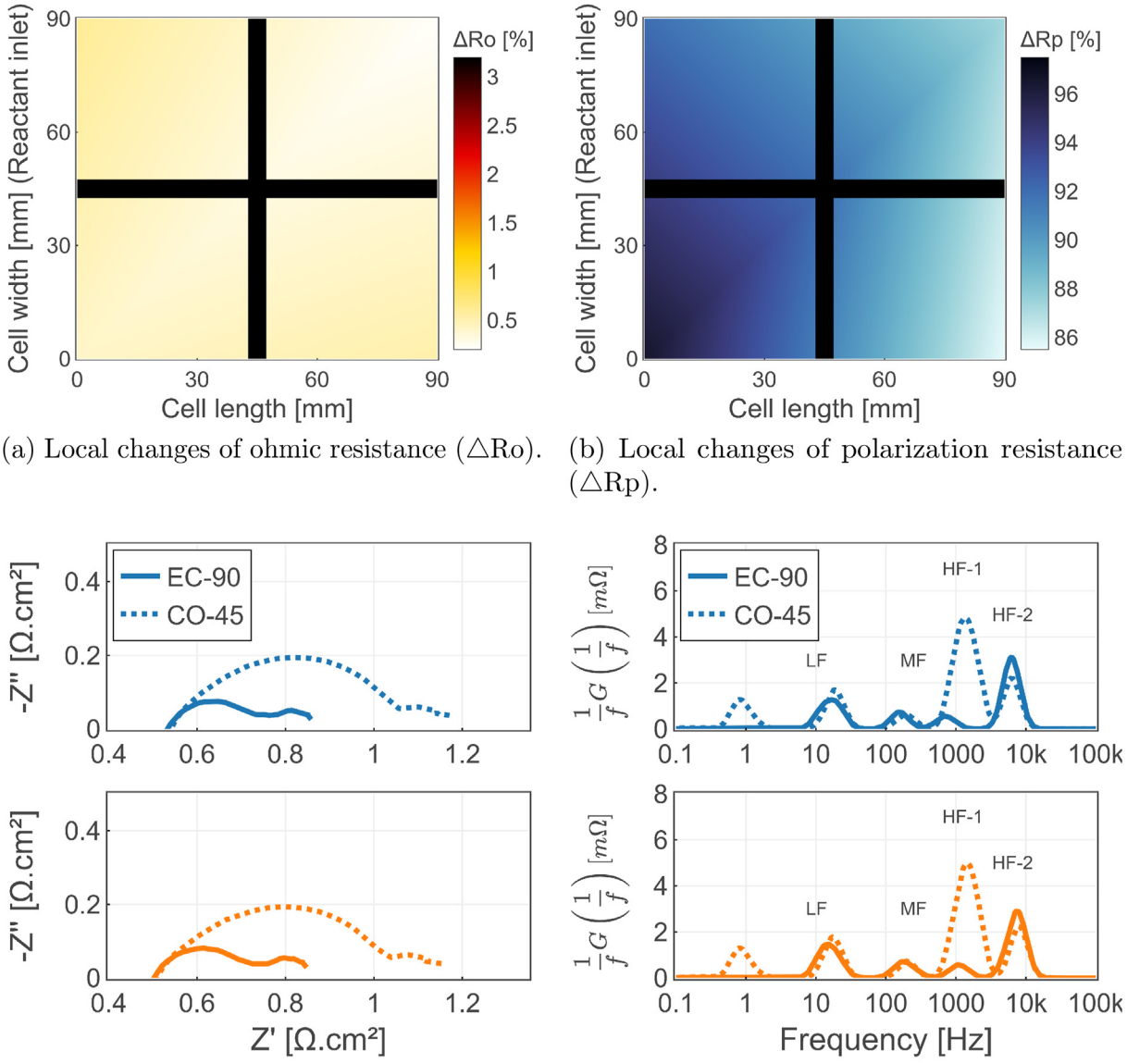

(a) Local changes of ohmic resistance (△Ro).

(b) Local changes of polarization resistance (△Rp).

(c) EIS at different CO_2 contents (L-1: top/blue, R-2: bottom/orange).

(d) DRT at different CO_2 contents (L-1: top/blue, R-2: bottom/orange).

Fig. 6 – Influence of increasing CO_2 content at 300 mA/cm^2 and 750 °C (EC-90/CO-45). (For interpretation of the references to color/colour in this figure legend, the reader is referred to the Web version of this article).

cell area was observed when switching from steam to co-electrolysis operation (Fig. 6a). Differently, a large increase of the polarization resistance was observed with slightly higher values for the gas inlet segments (Fig. 6b). Fig. 6c shows an increase of both, the low and high frequency arcs.

The LF peaks of both segments slightly shifted from 15 to 18 Hz with increasing amplitudes with substitution of H_2O with CO_2. Higher absolute amplitude values were observed for the outlet segment but higher changes at inlet segment. Again the occurrence of an additional peak at 1 Hz was observed whereby the amplitude was significantly higher compared to the previous experiment with increasing H_2O/H_2-ratio. The MF peaks stayed mostly unchanged. The first HF peak for EC-90 was located at 724 Hz for the inlet segment L-1 and at 1084 Hz for the outlet segment R-2. The first HF peak for CO-45 was located at 1084 Hz for L-1 and at 1418 Hz for R-2. Similar to the trend of LF peaks, higher amplitudes and frequencies were observed for the outlet segment, with uniform rates of change. The second HF peak for EC-90 was located at 6.1 kHz for L-1 and at 6.3 kHz for R-2. The second HF peak for CO-45 shifted to 7.5 kHz for L-1 and 8.0 kHz for R-2. Similar to the trend of the LF peaks, a more pronounced change of the amplitude was observed for the inlet segment with changing gas composition.

The uniform change in ohmic resistance could most likely be related to the locally canceling interactions between the different potentials of the endothermic electrolysis of H_2O and CO_2, different heat-generating irreversible overvoltage losses, and the reaction rate of the water-gas shift reaction (WGSR) along the cell length [21]. The high absolute increase of the polarization resistance compared to the previous experiment and the relatively higher change of the polarization resistance at the inlet segments with the changes of the process specific DRT peaks can be linked to different phenomena. Generally, the concentration overpotential, which summarized transport losses between the gas channel and the TPB [66], is considered lower for steam electrolysis than for CO_2-electrolysis [21,63]. The resulting steeper hydrogen gradient along the cell length (compared to CO) and the lower diffusivity of CO also lead to a positive reaction rate of the WGSR [67,68]. At these operating temperatures a relatively higher reaction rate can be expected for in the inlet regions of the cell [21]. Comparably changes of the steam electrode specific DRT peaks were observed during electrolysis operation with different H_2O/CO_2-ratios and were linked to increasing conversion, diffusion and charge transfer losses [48,65]. The dominant changes in these DRT peaks at approx. 1 kHz, 20 Hz and the newly formed peak at 1 Hz were interpreted as the result of a combination of higher mass transfer, diffusion and conversion losses during co-electrolysis operation as well as effects of the WGSR. In the inlet areas of the cell, where CO is practically absent, the CO_2 electrolysis reaction is less favored, with a competing temperature-depended WGSR [21] and a higher change for adsorption of carbonaceous species [23]. This likely resulted in an unstable equilibrium which is one of the determining factors for the higher local changes in polarization resistance. At overall conversion of the inlet gas mixture and the local less dominant effect of the WGSR towards the outlet segments of the cell result in a more stable local equilibrium with lower local losses.

Influence of temperature

Fig. 7 presents the results from steam electrolysis operation at 300 mA/cm^2 and different operating temperatures. Decreasing the operating temperature from 800 to 750 °C resulted in a significant increase of the ohmic resistance with relatively higher changes measured at the outlet segments (Fig. 7a). Differently the polarization resistance only presented a small increase with no significant gradient over the cell area (Fig. 7b).

The LF peaks of both segments remained mostly unchanged. The MF and HF peaks between 0.1 and 10 kHz also only present small changes with the MF peaks of both segments shifted towards slightly higher frequencies and higher amplitudes. The HF peaks of both segments no longer show a clear separation when decreasing the temperature, with the observed changes being basically identical for both segments. The shift of the MF peak towards higher frequencies was interpreted to possibly indicate the increasing influence of the ionic exchange processes over O_2 diffusivity processes with the increasing amplitude being the result of decreasing ionic conductivity of LSCF [47,61]. However, because of the very small changes in these frequency ranges, which can cover both air-electrode and fuel-electrode processes [48], the changes cannot be completely attributed to just one of these processes. The shift of the HF peaks to the intervening frequency range was associated with a slightly stronger influence of the gas diffusion processes compared to the other TPB processes characteristic of this frequency range. Decreasing temperature in steam electrolysis mode mainly increased the ohmic resistance as a result of decreasing electronic conductivity and decreasing ionic conductivity of YSZ and LSCF with the DRT peaks between 0.1 and 10 kHz presenting a certain dependency on the operation temperature as well as similar to the results presented in Ref. [47]. The relatively higher increase in ohmic resistance at the outlet segments was mainly associated with the approximately 5 °C steeper temperature gradient across the cell length during operation at 800 °C.

Fig. 8 presents the results from co-electrolysis operation at 300 mA/cm^2 and different operating temperatures. Similar to steam electrolysis operation, the ohmic resistance increased with relatively higher changes measured at the outlet segments when decreasing the operating temperature from 800 to 750 °C (Fig. 8a). Differently to steam electrolysis operation, the polarization resistance presented a significant increase whereby relatively higher changes were observed for the inlet segments (Fig. 8b). The LF peak of the inlet segment (L-1) shifts from 5 Hz to 1.27 mΩ towards a wider frequency range between 3 and 12 Hz with two main peaks at 0.8 and 4 Hz. Differently, the LF peak of the outlet segment (R-2) shifts from 5 Hz to 1.66 mΩ to 7 Hz and 1.24 mΩ when decreasing operating temperature from 800 to 750 °C. The MF peaks presented a comparable increase of amplitude for both segments but a significantly more pronounced shift towards lower frequencies for the L-1 segment. The HF peaks at 545 Hz merges with the other HF peaks at 4.5 kHz over a wide frequency range between 0.5 and 10 kHz, with a slightly wider frequency window for the outlet segment.

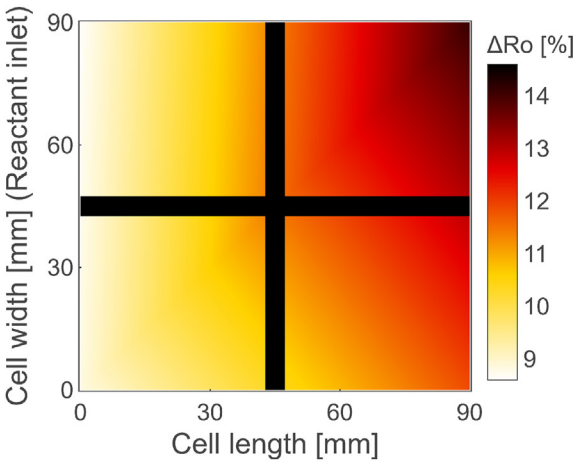

(a) Local changes of ohmic resistance (△Ro).

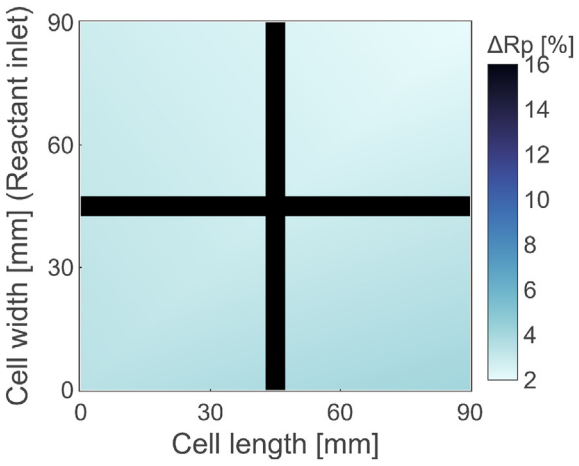

(b) Local changes of polarization resistance (△Rp).

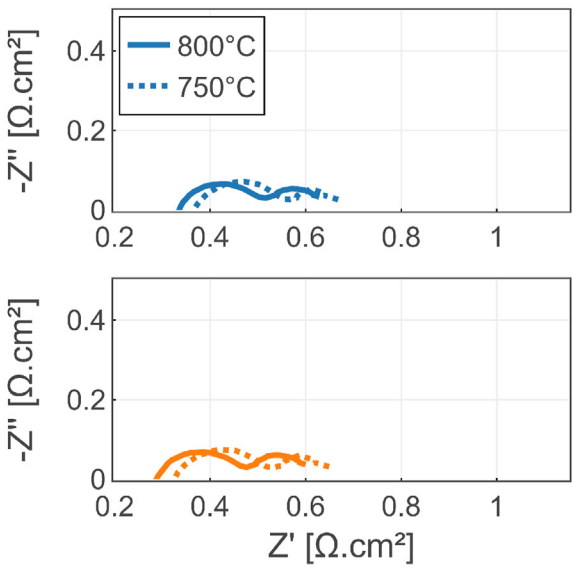

(c) EIS at different temperatures (L-1: top/blue, R-2: bottom/orange).

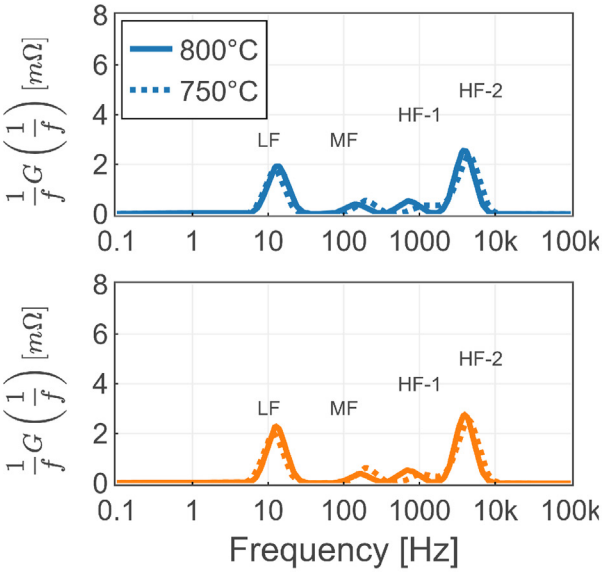

(d) DRT at different temperatures (L-1: top/blue, R-2: bottom/orange).

Fig. 7 – Influence of decreasing temperature at EC-50 and 300 mA/cm^2. (For interpretation of the references to color/colour in this figure legend, the reader is referred to the Web version of this article).

It can be seen that decreasing operating temperature significantly affects the polarization resistance in co-electrolysis operation compared to steam electrolysis operation, although the effect of temperature on ohmic resistance is comparable. The increase of the impedance with decreasing temperature can be mainly linked to decreasing electronic and ionic conductivity with inhibited steam electrode TPB processes [47]. The very high absolute increase of the polarization resistance compared to steam electrolysis can be further linked to an increase in mass transfer, diffusion and conversion losses in the steam electrode for co-electrolysis of H_2O and CO_2 [48,65]. Generally, the difference in potentials for electrolysis of H_2O and CO_2 is reduced at lower temperatures as a result of the lower equilibrium potential under standard conditions of CO_2-electrolysis compared to steam electrolysis [21,69]. The authors in Ref. [21] also describe that the WGSR reaction rates are significantly higher at higher temperatures and locally at the inlet areas of a cell. According to their research, the gradient of the WGSR reaction rates along the cell length is also higher, even leading to a strongly reversed WGSR at temperatures of 800 °C at the outlet areas of the cell. Therefore, the effect of decreasing temperature during co-electrolysis operation was assumed to be influenced not only by lower electronic and ionic conductivity [47] and lower electrolysis reaction rates, but also by the strongly locally dependent WGSR [21].

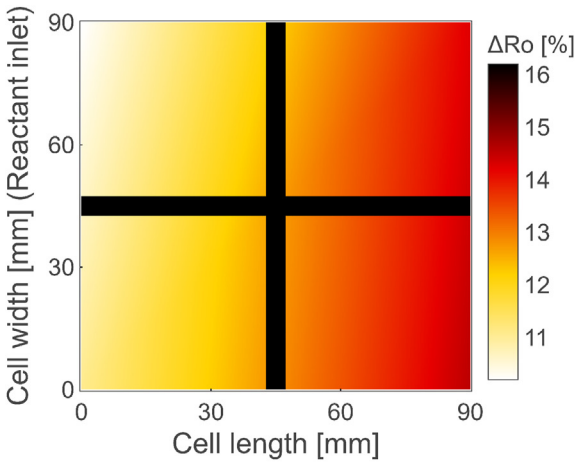

(a) Local changes of ohmic resistance (△Ro).

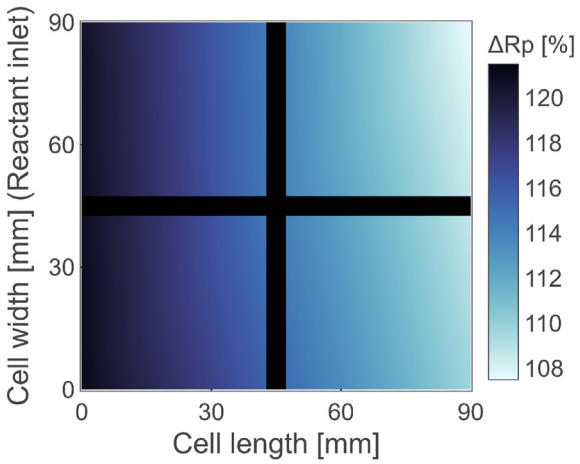

(b) Local changes of polarization resistance (△Rp).

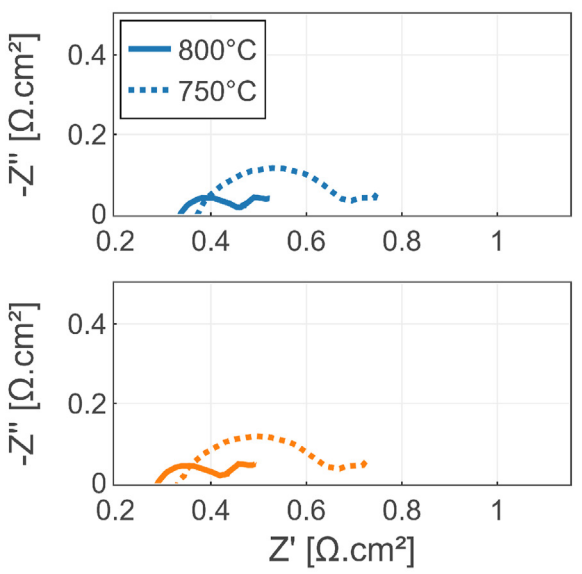

(c) EIS at different temperatures (L-1: top/blue, R-2: bottom/orange).

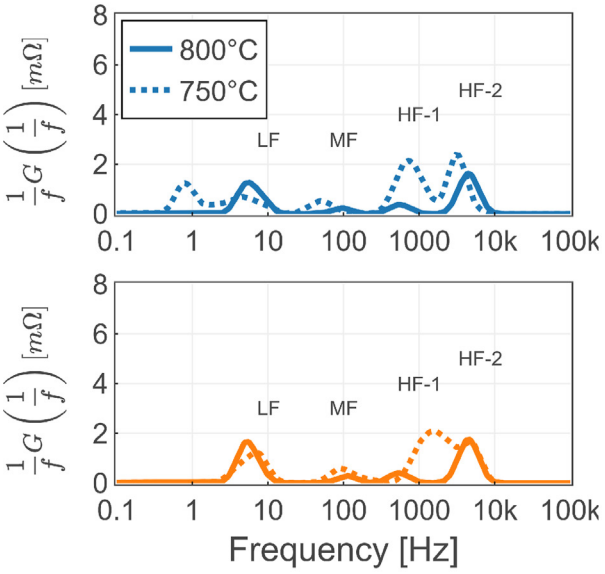

(d) DRT at different temperatures (L-1: top/blue, R-2: bottom/orange).

Fig. 8 – Influence of decreasing temperature at CO-25 and 300 mA/cm^2. (For interpretation of the references to color/colour in this figure legend, the reader is referred to the Web version of this article).

Short-term degradation

Fig. 9 presents the results of 66 h of operation at CC-90, 250 mA/cm^2 and 750 °C. The mean cell voltage increased by 14.0% from 1.172 to 1.336 V and the measured cell temperatures for the four segments increased by about 1 °C. The ohmic resistance R_O stay mostly unchanged with a minimal gradient along the diagonal of the cell surface. Differently, the polarization resistance R_P increased drastically, with increasing intensity at the fuel inlet areas (L-1/R-1) as presented in Fig. 9c. The changes visible in Fig. 9d could be interpreted to be linked to inhibited TPB processes within the steam electrode according to Refs. [64,65]. The authors in Ref. [23] state that the build-up of a solid phase such as carbon can negatively affect the catalytically active sites, porosity and tortuosity. The deposition of carbon is also reported to block gas pores which leads to inhibited electrochemical reactions and gas distribution within the steam electrode [30]. The authors in Refs. [10,70] discuss similar changes of the high frequency processes to be caused by deposition of impurities within the steam electrode. Nevertheless, the observed changes were not irreversible since the cell could also be reactivated within 24 h by regenerative operation with an H_2O/H_2 ratio of 4 at OCV. The authors in Ref. [57] also report that carbon formation within the steam electrode affects cell performance but may not lead to irreversible degradation, whereas complete

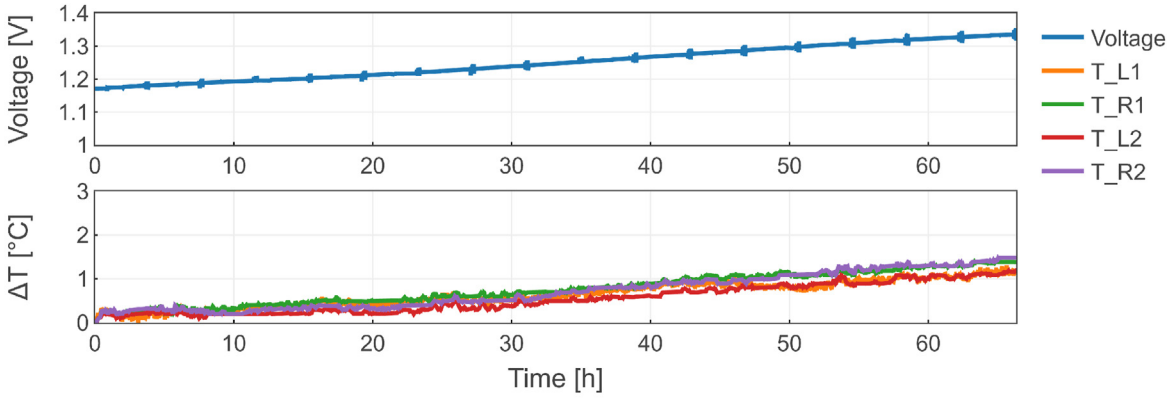

(a) Mean cell voltage and local temperature changes.

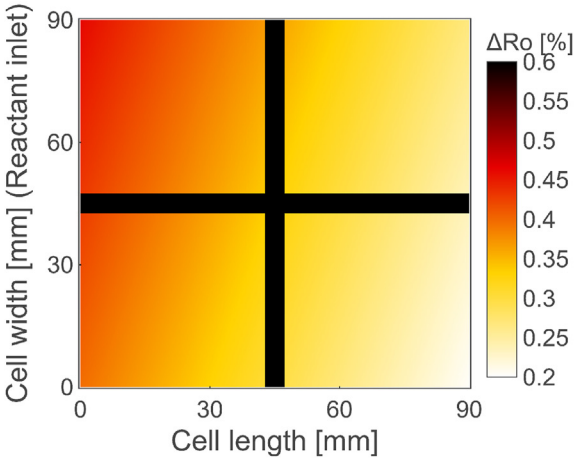

(b) Local changes of ohmic resistance (△Ro).

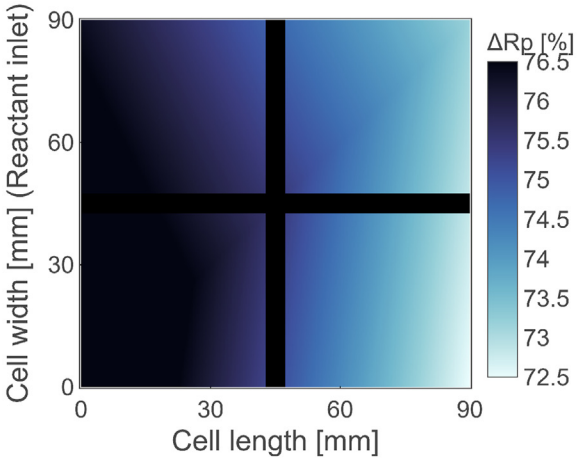

(c) Local changes of polarization resistance (△Rp).

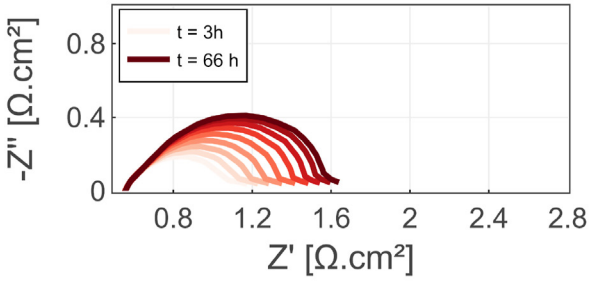

(d) Evolution of EIS curves (L-1).

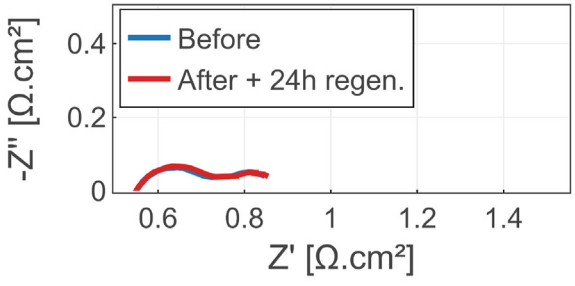

(e) Regeneration of performance at EC-90 and 250 mA/cm^2.

Fig. 9 – Short-term experiment at CC-90, 250 mA/cm^2 and 750 °C.

removal of solid carbon may take several hours if the carbon was identified at an reversible stage. The relatively stable ohmic resistance during operation at CC-90 indicates no significant structural damage to electrode/electrolyte interface as a consequence of potential coke formation according to Ref. [70].

Fig. 10 presents the results of 66 h of operation at CC-90, 150 mA/cm^2 and lower temperatures of 700 °C. Thereby, the mean cell voltage increased by 12.6% from 1.234 to 1.390 V and the measured cell temperatures for the four segments increased again by less than 1 °C. The ohmic resistance R_O slightly increased by 0.6–1.0% with a steeper gradient along

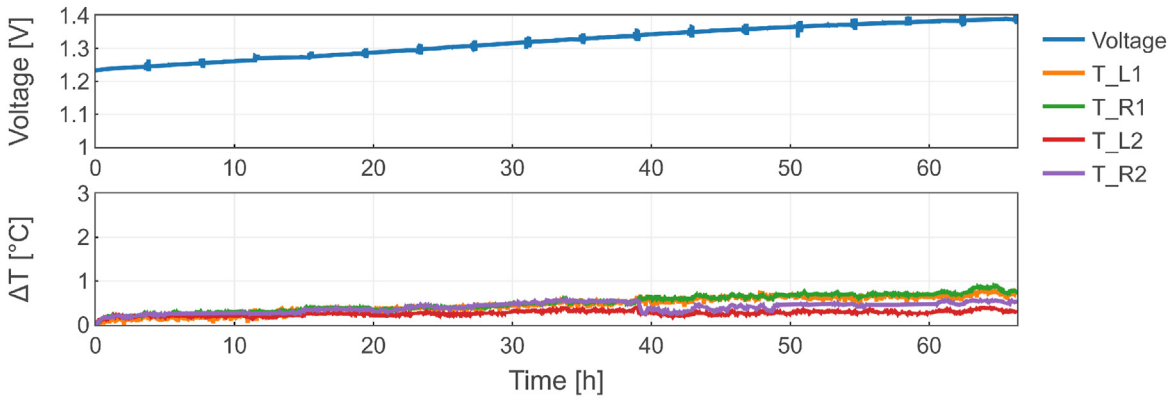

(a) Mean cell voltage and local temperature changes.

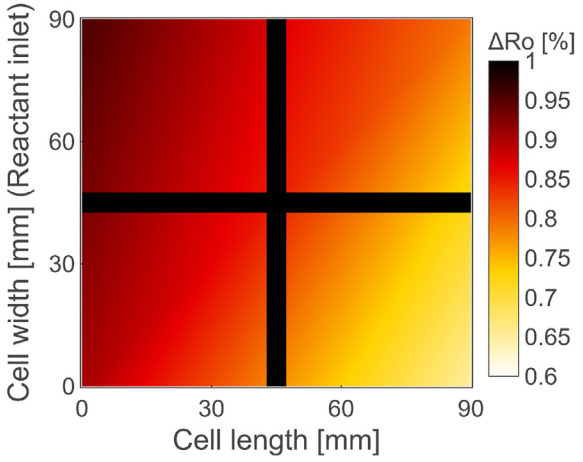

(b) Local changes of ohmic resistance (△Ro).

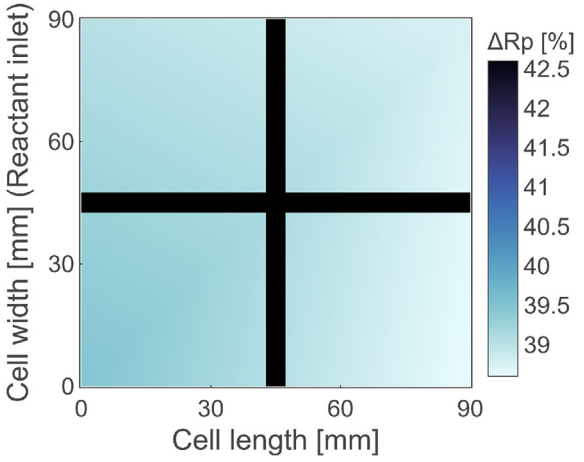

(c) Local changes of polarization resistance (△Rp).

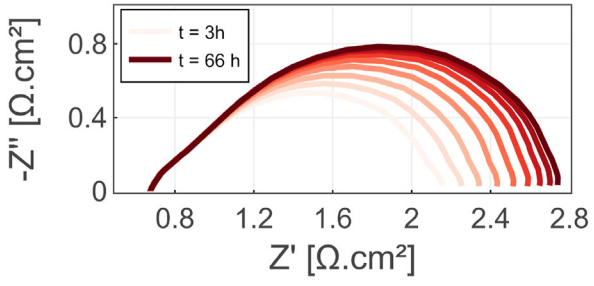

(d) Evolution of EIS curves (L-1).

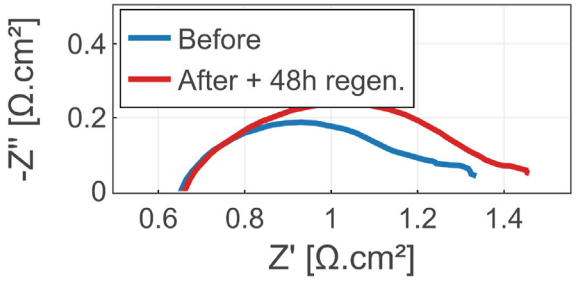

(e) Regeneration of performance at EC-90 and 250 mA/cm^2.

Fig. 10 – Short-term experiment at CC-90, 150 mA/cm^2 and 700 °C.

the diagonal of the cell surface compared to the previous experiment at 750 °C. Also, the polarization resistance R_P increased less dramatically and uniformly over the whole cell area. After this experiment the cell could not be fully reactivated within 48 h by regenerative operation with an H_2O/H_2 ratio of 4 at OCV as visible in Fig. 10e. After 120 h of regeneration operation, the cell appeared to have nearly recovered, although a slight deviation from the initial condition was still apparent for the fuel outlet segments (L-2/R-2). The authors in Ref. [23] also point out that the regeneration time for carbon gasification increases nonlinearly with a decrease in temperature, with an increasing amount of steam

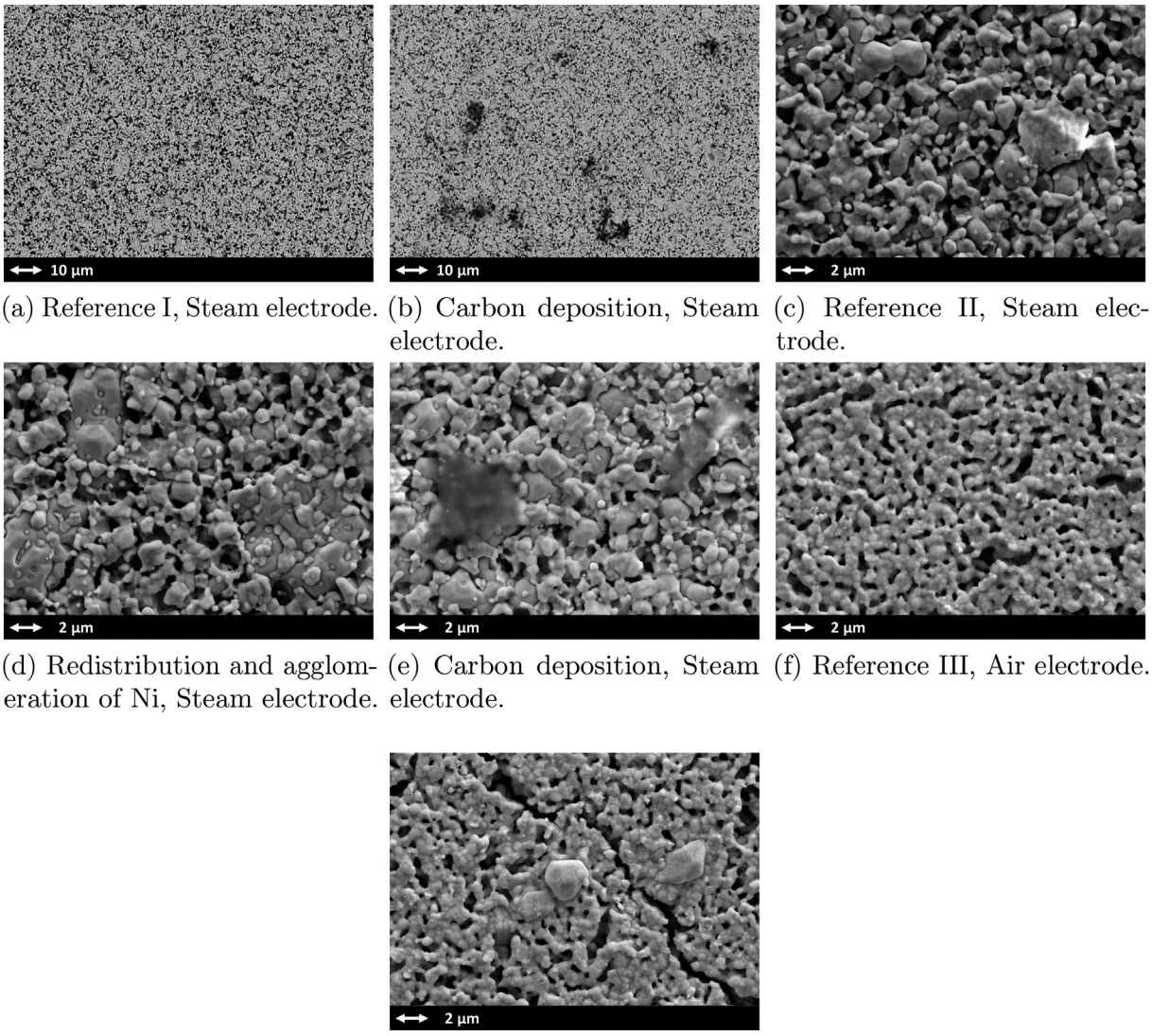

(a) Reference I, Steam electrode. (b) Carbon deposition, Steam electrode. (c) Reference II, Steam electrode.

(d) Redistribution and agglomeration of Ni, Steam electrode. (e) Carbon deposition, Steam electrode. (f) Reference III, Air electrode.

(g) Local grain growth, Air electrode.

Fig. 11 – Overview SEM analysis.

slightly accelerating the process in the case of reversible degradation, although 100% regeneration is not always possible. Most of the carbon deposits visible in Fig. 11b/11e could possibly be related to residues from operation at these operating conditions. A significantly higher density of carbon deposits was observed at the fuel outlet segments, indicating lower re-regeneration rates in these areas.

SEM analysis

Fig. 11 presents an excerpt of the results from the SEM analysis performed with the tested cells. Fig. 11a/11c/11f present a reference for the health state of the cell. SEM analysis of all cells presented Ni redistribution and Ni agglomeration (Fig. 11d), as they usually occur after electrolysis experiments [13,28]. SEM and EDS analysis of the cell operated in co-electrolysis mode for the short-term degradation experiments showed carbon deposits (Fig. 11b/11e). Some localized cases of grain growth on the air electrode were also noted, which were not linked to any particular phenomenon due to the very low frequency thereof (Fig. 11g). Although thermodynamics do not predict carbon formation, carbon formation can be a question of kinetics and local processes according to Refs. [71–74]. The authors in Ref. [71] further state that a low porosity of the steam electrode increases the risk of carbon formation. With decreasing porosity within the steam electrode as a result of Ni agglomeration and redistribution, it would be conceivable that these local carbon deposition occurred due to locally low CO_2/CO-ratios during operation at 700 °C.

Conclusion

In this study, locally resolved impedance and degradation characteristics were determined for SOECs operating in steam

and co-electrolysis modes. For this case, steam-electrode SOECs with segmented air electrodes were tested under different operating conditions, whereby different types and degrees of effects on the performance of the cells were observed and analyzed in detail. Significant correlations between local effects, operating conditions, electrode processes and degradation mechanisms were identified through electrochemical impedance spectroscopy (EIS), analysis via distribution of relaxation times (DRT) and scanning electron microscopy (SEM). The results presented quite different local phenomena for steam and co-electrolysis. The main influences on ohmic resistance can be summarized as changes due to temperature-related effects and thus inhibited electronic conductivity and decreasing ionic conductivity of the cell materials. In addition, a relatively higher increase in ohmic resistance at the outlet segments was associated with a steeper temperature gradient across the cell at higher temperatures. In general, polarization resistance showed a much stronger influence on changes in operating parameters such as current, input gas composition, and temperature in co-electrolysis operation compared to steam electrolysis operation. The gas inlet segments were significantly more affected. These changes were identified to be mainly linked to (i) a higher concentration overpotential for co-electrolysis than steam electrolysis and local CO_2/CO-ratio dependent mass transfer and diffusion losses and (ii) species and temperature dependent local reaction rate of the water-gas shift reaction (WGSR). Short-term degradation experiments during co-electrolysis showed the formation of local carbon deposits, possibly due to unfavorable reaction kinetics and locally occurring reactions. In addition, microstructural changes which lead to a decrease in porosity of the steam electrode were observed, which could create favorable conditions for carbon deposition at locally low CO_2/CO ratios and low temperatures. Therefore, it is recommended to adjust the inlet gas composition, current density and temperature for co-electrolysis mode in a way that the operational point is far from the theoretical carbon threshold. In addition, the application and further development of appropriate degradation mitigation strategies is recommended to extend the lifetime of the technology under challenging operating conditions. Nevertheless, negative cumulative influences due to the succession of several experiments must be considered and additional experiments are suggested to further verify the presented conclusions under additional operating conditions.

Declaration of competing interest

The authors declare that they have no known competing financial interests or personal relationships that could have appeared to influence the work reported in this paper.

Acknowledgement

The authors gratefully acknowledge the funding of the project "Degradation monitoring and performance optimisation of SOECs" (project number I 3994) by Austrian Science Fund (FWF). The cell manufacturing team at IEK-1 of Forschungszentrum Jülich is acknowledged for the cell fabrication.

Glossary of symbols

SOEC/EC	Solid oxide electrolysis cell
SOFC/FC	Solid oxide fuel cell
Ni − YSZ	Nickel
YSZ	Yttria-stabilized zirconia
LSCF	Lanthanum strontium cobalt ferrite
H_2	Hydrogen
H_2O	Water/Steam
CO	Carbon monoxide
CO_2	Carbon dioxide
O_2	Oxygen
O^{2-}	Oxygen-ion
WGSR	Water gas shift reaction
TPB	Triple phase boundary
OCV	Open circuit voltage
R_O	Ohmic resistance
R_P	Polarization resistance
SLPM	Standard litres per minute
EIS	Electrochemical impedance spectroscopy
DRT	Distribution od relaxation times
KK	Kramers-Kronig
SEM	Scanning electron microscope
EDS	Energy dispersive X-ray

REFERENCES

[1] IPCC. Assessment report 6 climate change 2021: the physical science basis. 2021. https://www.ipcc.ch/report/ar6/wg1/.
[2] Laguna-Bercero M. Recent advances in high temperature electrolysis using solid oxide fuel cells: a review. J Power Sources 2012;203:4–16. https://doi.org/10.1016/j.jpowsour.2011.12.019.
[3] Kovac A, Paranos M, Marcius D. Hydrogen in energy transition: a review. Int J Hydrogen Energy 2021;46:10016–35. https://doi.org/10.1016/j.ijhydene.2020.11.256. https://www.sciencedirect.com/science/article/pii/S0360319920345079 [hydrogen and Fuel Cells].
[4] Mogensen MB, Chen M, Frandsen HL, Graves C, Hansen JB, Hansen KV, Hauch A, Jacobsen T, Jensen SH, Skafte TL, Sun X. Reversible solid-oxide cells for clean and sustainable energy. Clean Energy 2019;3:175–201. https://doi.org/10.1093/ce/zkz023.
[5] Lo Faro M, Trocino S, Zignani SC, Antonucci V, Aricò AS. Production of syngas by solid oxide electrolysis: a case study. Int J Hydrogen Energy 2017;42:27859–65. https://doi.org/10.1016/j.ijhydene.2017.06.157.
[6] Posdziech O, Schwarze K, Brabandt J. Efficient hydrogen production for industry and electricity storage via high-temperature electrolysis. Int J Hydrogen Energy 2019;4:19089–101. https://doi.org/10.1016/j.ijhydene.2018.05.169.
[7] Nielsen AS, Ostadi M, Austbø B, Hillestad M, del Alamo G, Burheim O. Enhancing the efficiency of power- and biomass-to-liquid fuel processes using fuel-assisted solid oxide electrolysis cells. Fuel 2022;321:123987. https://doi.org/10.1016/j.fuel.2022.123987. doi:10.1016/j.fuel.2022.123987.

[8] Hauch A, Küngas R, Blennow P, Hansen AB, Hansen JB, Mathiesen BV, Mogensen MB. Recent advances in solid oxide cell technology for electrolysis. Science 2020;370. https://doi.org/10.1126/science.aba6118.
[9] Subotić V, Hochenauer C. Analysis of solid oxide fuel and electrolysis cells operated in a real-system environment: state-of-the-health diagnostic, failure modes, degradation mitigation and performance regeneration. Prog Energy Combust Sci 2022;93. https://doi.org/10.1016/j.pecs.2022.101011.
[10] Graves C, Ebbesen SD, Mogensen M. Co-electrolysis of CO2 and H2O in solid oxide cells: performance and durability. Solid State Ionics 2011;192:398–403. https://doi.org/10.1016/j.ssi.2010.06.014.
[11] Fang Q, Blum L, Menzler NH, Stolten D. Solid oxide electrolyzer stack with 20,000 h of operation. ECS Trans 2017;78:2885–93. https://doi.org/10.1149/07801.2885ecst.
[12] Subotić V, Thaller T, Königshofer B, Menzler NH, Bucher E, Egger A, Hochenauer C. Performance assessment of industrial-sized solid oxide cells operated in a reversible mode: detailed numerical and experimental study. Int J Hydrogen Energy 2020;45:29166–85. https://doi.org/10.1016/j.ijhydene.2020.07.165.
[13] Subotic V, Königshofer B, Juricic D, Kusnezoff M, Schröttner H, Hochenauer C, Boskoski P. Detailed insight into processes of reversible solid oxide cells and stacks using drt analysis. Energy Convers Manag 2020;226. https://doi.org/10.1016/j.enconman.2020.113509.
[14] Song S, Xiong X, Wu X, Xue Z. Modeling the SOFC by BP neural network algorithm. Int J Hydrogen Energy 2021;46:20065–77. https://doi.org/10.1016/j.ijhydene.2021.03.132. doi:10.1016/j.ijhydene.2021.03.132.
[15] Schluckner C, Subotić V, Lawlor V, Hochenauer C. Three-dimensional numerical and experimental investigation of an industrial-sized SOFC fueled by diesel reformat - Part I: creation of a base model for further carbon deposition modeling. Int J Hydrogen Energy 2014;39:19102–18. https://doi.org/10.1016/j.ijhydene.2014.09.108.
[16] Schluckner C, Subotić V, Lawlor V, Hochenauer C. Numerical SOFC anode catalyst occupation study: internal reforming of carbonaceous fuel mixtures. J Electrochem Soc 2016;163:F761–70. https://doi.org/10.1149/2.0061608jes.
[17] Stoeckl B, Subotić V, Preininger M, Schroettner H, Hochenauer C. SOFC operation with carbon oxides: experimental analysis of performance and degradation. Electrochim Acta 2018;275:256–64. https://doi.org/10.1016/j.electacta.2018.04.036.
[18] Bessler WG, Gewies S, Willich C, Schiller G, Friedrich KA. Spatial distribution of electrochemical performance in a segmented SOFC: a combined modeling and experimental study. Fuel Cell 2010;10:411–8. https://doi.org/10.1002/fuce.200900083.
[19] Blum L, Packbier U, Vinke IC, De Haart LG. Long-term testing of SOFC stacks at forschungszentrum jülich. Fuel Cell 2013;13:646–53. https://doi.org/10.1002/fuce.201200151.
[20] Schluckner C, Subotić V, Preißl S, Hochenauer C. Numerical analysis of flow configurations and electrical contact positions in SOFC single cells and their impact on local effects. Int J Hydrogen Energy 2019;44:1877–95. https://doi.org/10.1016/j.ijhydene.2018.11.132.
[21] Ni M. 2D thermal modeling of a solid oxide electrolyzer cell (SOEC) for syngas production by H2O/CO2 co-electrolysis. Int J Hydrogen Energy 2012;37:6389–99. https://doi.org/10.1016/j.ijhydene.2012.01.072. doi:10.1016/j.ijhydene.2012.01.072.
[22] Schluckner C, Subotić V, Lawlor V, Hochenauer C. Three-dimensional numerical and experimental investigation of an industrial-sized SOFC fueled by diesel reformat - Part II: detailed reforming chemistry and carbon deposition analysis. Int J Hydrogen Energy 2015;40:10943–59. https://doi.org/10.1016/j.ijhydene.2015.06.024.
[23] Schluckner C, Subotić V, Lawlor V, Hochenauer C. CFD-simulation of effective carbon gasification strategies from high temperature SOFC Ni–YSZ cermet anodes. Int J Hydrogen Energy 2017;42:4434–48. https://doi.org/10.1016/j.ijhydene.2016.11.162.
[24] Nakajo A, Mueller F, Brouwer J, Van Herle J, Favrat D. Mechanical reliability and durability of SOFC stacks. Part I: modelling of the effect of operating conditions and design alternatives on the reliability. Int J Hydrogen Energy 2012;37:9249–68. https://doi.org/10.1016/j.ijhydene.2012.03.043. doi:10.1016/j.ijhydene.2012.03.043.
[25] Nakajo A, Mueller F, Brouwer J, Van Herle J, Favrat D. Mechanical reliability and durability of SOFC stacks. Part II: modelling of mechanical failures during ageing and cycling. Int J Hydrogen Energy 2012;37:9269–86. https://doi.org/10.1016/j.ijhydene.2012.03.023. doi:10.1016/j.ijhydene.2012.03.023.
[26] Canavar M, Mat A, Celik S, Timurkutluk B, Kaplan Y. Investigation of temperature distribution and performance of SOFC short stack with/without machined gas channels. Int J Hydrogen Energy 2016;41:10030–6. https://doi.org/10.1016/j.ijhydene.2016.02.045. doi:10.1016/j.ijhydene.2016.02.045.
[27] Seo KD, Kim YJ, young Park J, Lim HT. Investigating the effect of current collecting conditions on solid oxide fuel cell (SOFC) performance with additional voltage probes. Int J Hydrogen Energy 2018;43:2349–58. https://doi.org/10.1016/j.ijhydene.2017.11.109. doi:10.1016/j.ijhydene.2017.11.109.
[28] Königshofer B, Pongratz G, Nusev G, Boškoski P, Höber M, Juričić D, Kusnezoff M, Trofimenko N, Schröttner H, Hochenauer C, Subotić V. Development of test protocols for solid oxide electrolysis cells operated under accelerated degradation conditions. J Power Sources 2021;497. https://doi.org/10.1016/j.jpowsour.2021.229875.
[29] Königshofer B, Boškoski P, Nusev G, Koroschetz M, Hochfellner M, Schwaiger M, Juričić D, Hochenauer C, Subotić V. Performance assessment and evaluation of SOC stacks designed for application in a reversible operated 150 kW rSOC power plant. Appl Energy 2021;283. https://doi.org/10.1016/j.apenergy.2020.116372.
[30] Subotić V, Schluckner C, Strasser J, Lawlor V, Mathe J, Rechberger J, Schroettner H, Hochenauer C. In-situ electrochemical characterization methods for industrial-sized planar solid oxide fuel cells Part I: methodology, qualification and detection of carbon deposition. Electrochim Acta 2016;207:224–36. https://doi.org/10.1016/j.electacta.2016.05.025.
[31] Höber M, Wachter P, Königshofer B, Mütter F, Schröttner H, Hochenauer C, Subotić V. In operando electrochemical impedance spectroscopy monitoring of nickel catalysts for hydrogen production, Part I: methodology and performance characterization. Fuel 2022;324:124256. https://linkinghub.elsevier.com/retrieve/pii/S001623612201105X. doi:10.1016/j.fuel.2022.124256.
[32] Lang M, Raab S, Lemcke MS, Bohn C, Pysik M. Long term behavior of solid oxide electrolyser (soec) stacks. ECS Trans 2019;91:2713–25. https://doi.org/10.1149/09101.2713ecst.
[33] Comminges C, Fu QX, Zahid M, Steiner NY, Bucheli O. Monitoring the degradation of a solid oxide fuel cell stack during 10,000 h via electrochemical impedance spectroscopy. Electrochim Acta 2012;59:367–75. https://doi.org/10.1016/j.electacta.2011.10.080.
[34] Königshofer B, Höber M, Nusev G, Boškoski P, Hochenauer C, Subotić V. Accelerated degradation for solid oxide electrolysers : analysis and prediction of performance for varying operating environments. J Power Sources

2022;523:230982. https://doi.org/10.1016/j.jpowsour.2022.230982. doi:10.1016/j.jpowsour.2022.230982.
[35] Subotić V, Stoeckl B, Lawlor V, Strasser J, Schroettner H, Hochenauer C. Towards a practical tool for online monitoring of solid oxide fuel cell operation: an experimental study and application of advanced data analysis approaches. Appl Energy 2018;222:748–61. https://doi.org/10.1016/j.apenergy.2018.03.182.
[36] Schlüter N, Ernst S, Schröder U. Finding the optimal regularization parameter in distribution of relaxation times analysis. Chemelectrochem 2019;6:6027–37. https://onlinelibrary.wiley.com/doi/abs/10.1002/celc.201901863. doi:10.1002/celc.201901863.
[37] Fang Q, Blum L, Menzler NH. Performance and degradation of solid oxide electrolysis cells in stack. J Electrochem Soc 2015;162:F907–12. https://doi.org/10.1149/2.0941508jes.
[38] Yan Y, Fang Q, Blum L, Lehnert W. Performance and degradation of an soec stack with different cell components. Electrochim Acta 2017;258:1254–61. https://doi.org/10.1016/j.electacta.2017.11.180.
[39] Dierickx S, Weber A, Ivers-Tiffée E. How the distribution of relaxation times enhances complex equivalent circuit models for fuel cells. Electrochim Acta 2020;355:136764. https://doi.org/10.1016/j.electacta.2020.136764.
[40] Zhang T, Zhao Y, Zhang X, Zhang H, Yu N, Liu T, Wang Y. Thermal stability of an in situ exsolved metallic nanoparticle structured perovskite type hydrogen electrode for solid oxide cells. ACS Sustainable Chem Eng 2019;7:17834–44. https://doi.org/10.1021/acssuschemeng.9b04350.
[41] Knibbe R, Traulsen ML, Hauch A, Ebbesen SD, Mogensen M. Solid oxide electrolysis cells: degradation at high current densities. J Electrochem Soc 2010;157:B1209. https://doi.org/10.1149/1.3447752.
[42] Hjalmarsson P, Sun X, Liu YL, Chen M. Durability of high performance Ni-yttria stabilized zirconia supported solid oxide electrolysis cells at high current density. J Power Sources 2014;262:316–22. https://doi.org/10.1016/j.jpowsour.2014.03.133. doi:10.1016/j.jpowsour.2014.03.133.
[43] Jia C, Chen M, Han M. Performance and electrochemical analysis of solid oxide fuel cells based on LSCF-YSZ nano-electrode. Int J Appl Ceram Technol 2017;14:1006–12. https://doi.org/10.1111/ijac.12748.
[44] Rao M, Jensen SH, Sun X, Hagen A. Unwinding entangled degradation mechanisms in solid oxide electrolysis cells through electrode modifications and impedance analysis. Fuel Cell 2019;19:445–57. https://doi.org/10.1002/fuce.201800166.
[45] Yang Y, Tong X, Hauch A, Sun X, Yang Z, Peng S, Chen M. Study of solid oxide electrolysis cells operated in potentiostatic mode: effect of operating temperature on durability. Chem Eng J 2021;417:129260. https://doi.org/10.1016/j.cej.2021.129260.
[46] Leonide A, Sonn V, Weber A, Ivers-Tiffée E. Evaluation and modeling of the cell resistance in anode-supported solid oxide fuel cells. J Electrochem Soc 2008;155:B36. https://doi.org/10.1149/1.2801372.
[47] Caliandro P, Nakajo A, Diethelm S, Van herle J. Model-assisted identification of solid oxide cell elementary processes by electrochemical impedance spectroscopy measurements. J Power Sources 2019;436:226838. https://doi.org/10.1016/j.jpowsour.2019.226838.
[48] Rao M, Sun X, Hagen A. Durability of solid oxide electrolysis stack under dynamic load cycling for syngas production. J Power Sources 2020;451:227781. https://doi.org/10.1016/j.jpowsour.2020.227781. doi:10.1016/j.jpowsour.2020.227781.
[49] Meng X, Wang Y, Zhao Y, Zhang T, Yu N, Chen X, Miao M, Liu T. In-situ exsolution of nanoparticles from Ni substituted Sr2Fe1.5Mo0.5O6 perovskite oxides with different Ni doping contents. Electrochim Acta 2020;348:1–12. https://doi.org/10.1016/j.electacta.2020.136351.
[50] Sun X, Bonaccorso AD, Graves C, Ebbesen SD, Jensen SH, Hagen A, Holtappels P, Hendriksen PV, Mogensen MB. Performance characterization of solid oxide cells under high pressure. Fuel Cell 2015;15:697–702. https://doi.org/10.1002/fuce.201500020.
[51] Papurello D, Menichini D, Lanzini A. Distributed relaxation times technique for the determination of fuel cell losses with an equivalent circuit model to identify physicochemical processes. Electrochim Acta 2017;258:98–109. https://doi.org/10.1016/j.electacta.2017.10.052. https://linkinghub.elsevier.com/retrieve/pii/S0013468617321503.
[52] Sumi H, Shimada H, Yamaguchi Y, Yamaguchi T, Fujishiro Y. Degradation evaluation by distribution of relaxation times analysis for microtubular solid oxide fuel cells. Electrochim Acta 2020;339:135913. https://doi.org/10.1016/j.electacta.2020.135913.
[53] Sonn V, Leonide A, Ivers-Tiffée E. Combined deconvolution and cnls fitting approach applied on the impedance response of technical ni/8ysz cermet electrodes. J Electrochem Soc 2008;155:B675. https://doi.org/10.1149/1.2908860.
[54] Leonide A, Rüger B, Weber A, Meulenberg WA, Ivers-Tiffée E. Impedance study of alternative (La,Sr)FeO[sub 3-δ] and (La,Sr)(Co,Fe)O[sub 3-δ] MIEC cathode compositions. J Electrochem Soc 2010;157:B234. https://doi.org/10.1149/1.3265473.
[55] Rao M, Sun X, Hagen A. A comparative study of durability of solid oxide electrolysis cells tested for Co-electrolysis under galvanostatic and potentiostatic conditions. J Electrochem Soc 2018;165:F748–55. https://doi.org/10.1149/2.0151810jes.
[56] Subotić V, Schluckner C, Stöckl B, Lawlor V, Schroettner H, Hochenauer C. Strategy for carbon gasification from porous Ni-YSZ anodes of industrial-sized ASC-SOFCs and effects of carbon growth. J Electrochem Soc 2016;163:F1515–22. https://doi.org/10.1149/2.0521614jes.
[57] Subotic V, Schluckner C, Mathe J, Rechberger J, Schroettner H, Hochenauer C. Anode regeneration following carbon depositions in an industrial-sized anode supported solid oxide fuel cell operating on synthetic diesel reformate. J Power Sources 2015;295:55–66. https://doi.org/10.1016/j.jpowsour.2015.06.133.
[58] Agarwal P, Orazem ME, Garcia-Rubio LH. Application of measurement models to impedance spectroscopy iii. evaluation of consistency with the kramers-kronig relations. J Electrochem Soc 1995;142:4159–68.
[59] Ehm W, Kaus R, Strunz C-ASW. Z-hit : a simple relation between impedance modulus and phase angle. providing a new way to the validation of electrochemical impedance spectra. In: Mansfeld F, Huet F, Mattos O, editors. New trends in electrochemical impedance spectroscopy and electrochemical noise analysis. Electrochemical Society Inc; 2001. p. 1–10.
[60] Ciucci F, Chen C. Analysis of electrochemical impedance spectroscopy data using the distribution of relaxation times: a bayesian and hierarchical bayesian approach. Electrochim Acta 2015. https://doi.org/10.1016/j.electacta.2015.03.123.
[61] Königshofer B, Höber M, Boškoski P, Nusev G, Juričić D, Hochenauer C, Subotic V. Performance investigation and optimization of a SOEC stack operated under industrially relevant conditions. ECS Trans 2021;103:519–28. https://doi.org/10.1149/10301.0519ecst.
[62] Subotić V, Futamura S, Harrington GF, Matsuda J, Natsukoshi K, Sasaki K. Towards understanding of oxygen electrode processes during solid oxide electrolysis operation to improve simultaneous fuel and oxygen generation. J Power Sources 2021;492:229600. https://doi.org/10.1016/j.jpowsour.2021.229600.

[63] Wang Y, Liu T, Lei L, Chen F. High temperature solid oxide h2o/co2 co-electrolysis for syngas production. Fuel Process Technol 2017;161:248–58. https://doi.org/10.1016/j.fuproc.2016.08.009.
[64] Hauch A, Marchese M, Lanzini A, Graves C. Re-activation of degraded nickel cermet anodes - nano-particle formation via reverse current pulses. J Power Sources 2018;377:110–20. https://doi.org/10.1016/j.jpowsour.2017.11.088.
[65] Sun X, Liu Y, Hendriksen PV, Chen M. An operation strategy for mitigating the degradation of solid oxide electrolysis cells for syngas production. J Power Sources 2021;506:230136. https://doi.org/10.1016/j.jpowsour.2021.230136.
[66] Dincer I, Bicer Y. 2.1 ammonia. In: Dincer I, editor. Comprehensive energy systems. Oxford: Elsevier; 2018. p. 1–39. https://doi.org/10.1016/B978-0-12-809597-3.00201-7. https://www.sciencedirect.com/science/article/pii/B9780128095973002017.
[67] Ni M. Computational fluid dynamics modeling of a solid oxide electrolyzer cell for hydrogen production. Int J Hydrogen Energy 2009;34:7795–806. https://doi.org/10.1016/j.ijhydene.2009.07.080. doi:10.1016/j.ijhydene.2009.07.080.
[68] Ni M. Modeling of a solid oxide electrolysis cell for carbon dioxide electrolysis. Chem Eng J 2010;164:246–54. https://doi.org/10.1016/j.cej.2010.08.032. doi:10.1016/j.cej.2010.08.032.
[69] Ni M. An electrochemical model for syngas production by co-electrolysis of H 2O and CO 2. J Power Sources 2012;202:209–16. https://doi.org/10.1016/j.jpowsour.2011.11.080. doi:10.1016/j.jpowsour.2011.11.080.
[70] Ebbesen SD, Mogensen M. Electrolysis of carbon dioxide in solid oxide electrolysis cells. J Power Sources 2009;193:349–58. https://doi.org/10.1016/j.jpowsour.2009.02.093.
[71] Skafte TL, Blennow P, Hjelm J, Graves C. Carbon deposition and sulfur poisoning during CO2 electrolysis in nickel-based solid oxide cell electrodes. J Power Sources 2018;373:54–60. https://doi.org/10.1016/j.jpowsour.2017.10.097. doi:10.1016/j.jpowsour.2017.10.097.
[72] Tao Y, Ebbesen SD, Mogensen MB. Carbon deposition in solid oxide cells during Co-electrolysis of H 2 O and CO 2. J Electrochem Soc 2014;161:F337–43. https://doi.org/10.1149/2.079403jes.
[73] Han Z, Yang Z, Han M. Comprehensive investigation of methane conversion over Ni(111) surface under a consistent DFT framework: implications for anti-coking of SOFC anodes. Appl Surf Sci 2019;480:243–55. https://doi.org/10.1016/j.apsusc.2019.02.084. doi:10.1016/j.apsusc.2019.02.084.
[74] Duboviks V, Lomberg M, Maher RC, Cohen LF, Brandon NP, Offer GJ. Carbon deposition behaviour in metal-infiltrated gadolinia doped ceria electrodes for simulated biogas upgrading in solid oxide electrolysis cells. J Power Sources 2015;293:912–21. https://doi.org/10.1016/j.jpowsour.2015.06.003. doi:10.1016/j.jpowsour.2015.06.003.